

# High-performance Sources of Multidimensionally Engineered Quantum Light Based on Monolithic Microcavity-metalens Interfaces

Jiantao Ma<sup>1†</sup>, Dong Liu<sup>1†</sup>, Shunfa Liu<sup>1†</sup>, Jiawei Yang<sup>1†</sup>, Nilo Mata-Cervera<sup>2</sup>, Bo Chen<sup>1</sup>, Xueshi Li<sup>1</sup>, Guixin Qiu<sup>1</sup>, Kaixuan Chen<sup>3</sup>, Hanqing Liu<sup>4</sup>, Haiqiao Ni<sup>4</sup>, Dunzhao Wei<sup>1</sup>, Zhichuan Niu<sup>4</sup>, Ying Yu<sup>1</sup>, Yijie Shen<sup>2,5\*</sup>, Liu Liu<sup>6\*</sup>, Xuehua Wang<sup>1,7\*</sup>, Jin Liu<sup>1,7\*</sup>

<sup>1</sup>State Key Laboratory of Optoelectronic Materials and Technologies, School of Physics, School of Electronics and Information Technology, Sun Yat-sen University, Guangzhou, 510275, China

<sup>2</sup>Centre for Disruptive Photonic Technologies, School of Physical and Mathematical Sciences, Nanyang Technological University, Singapore 637371, Singapore

<sup>3</sup>Guangdong Provincial Key Laboratory of Optical Information Materials and Technology, South China Academy of Advanced Optoelectronics, South China Normal University, Guangzhou, 510006, China

<sup>4</sup>State Key Laboratory for Superlattices and Microstructures, Institute of Semiconductors, Chinese Academy of Sciences, Center of Materials Science and Optoelectronics Engineering, University of Chinese Academy of Sciences, Beijing, 100083, China

<sup>5</sup>School of Electrical and Electronic Engineering, Nanyang Technological University, Singapore 639798, Singapore

<sup>6</sup>State Key Laboratory for Modern Optical Instrumentation, College of Optical Science and Engineering, International Research Center for Advanced Photonics, Zhejiang University, Hangzhou, 310058, China

<sup>7</sup>Quantum Science Center of Guangdong–Hong Kong–Macao Greater Bay Area, Shenzhen, 518105, China

†These authors contributed equally to this work.

\*Corresponding author. Email: yijie.shen@ntu.edu.sg (Y.S.); liuliuopt@zju.edu.cn (L.L.); wangxueh@mail.sysu.edu.cn (X.W.); liujin23@mail.sysu.edu.cn (J.L.);

**Abstract:** The ultimate non-classic light sources for modern photonic quantum technology require on-demand generation of indistinguishable quantum light with high brightness and flexible engineering of quantum emission in multiple degrees of freedom. In this work, we present monolithic microcavity-metalens interfaces consisting of quantum-dot-micropillar single-photon sources and ultra-thin metalenses accurately aligned on opposite sides of an III-V compound semiconductor chip. The pronounced cavity quantum electrodynamics effect enabled by the micropillar cavity facilitates single-photon emission from quantum dots with simultaneous high degrees of single-photon purity, source brightness and photon indistinguishability while the multi-functional metalenses concurrently tailor quantum emission in multiple physical degrees of freedom including radiation divergence, emission directionality, polarization state and orbital angular momentum (OAM). Furthermore, high-fidelity polarization-OAM entanglement and single photons with local spin topologies are successfully generated in our integrated device. In particular, we demonstrate stable propagations of single-photon skyrmions in atmospheric turbulence and reveal their topological advantages over the conventional structured quantum

light. Our work advances the research fields of integrated quantum photonics and meta-optics, providing integrated high-dimensional quantum light sources for advanced photonic quantum science and technology.

## 1 Introduction:

Quantum radiation of light serves as a cornerstone for modern photonic quantum technology [1] with applications across quantum communication [2], quantum computing [3–5] and quantum metrology [6]. As the most prominent quantum state of light, single photons can be deterministically generated in two-level systems such as natural atoms [7], trapped ions [8] and solid-state quantum emitters [9]. Among them, solid-state quantum emitters, e.g., excitons in quantum dots (QDs) [10–12], defects in wide bandgap semiconductors [13,14] and layered materials [15], are particularly appealing for integrated quantum photonic technology [16,17] due to their compatibility with the modern nanofabrication process. To date, epitaxial QDs are leading the device performance of quantum light sources in terms of low multi-photon probability, record source brightness, high entanglement fidelity and near-unity photon indistinguishability [18–25] by harnessing the accelerated spontaneous emission rate and improved emission directionality empowered by the cavity quantum electrodynamics (cQED) effect. However, cavity-enhanced solid-state quantum light sources predominantly operate in the simplest Gaussian-like modes in linear polarization states [21,24,26,27], which limits their applications in high-dimensional quantum information processing involving manipulation of quantum emission in multiple degrees of freedom. Alternatively, broadband nanostructures have been widely employed for molding the flow of light [28,29]. In particular, metasurfaces provide an ultra-thin solution of flexibly tailoring photonic states in multiple degrees of freedom [29–31], which have been successfully implemented in the manipulation of quantum states of light by either having the quantum sources integrated [32–37] or separated [38–40] from the metasurfaces. Nevertheless, indistinguishable and bright quantum light sources have not been achieved in the metalens-quantum emitter platform due to the relatively weak light-matter interaction strength, i.e., limited Purcell effect, provided by metasurfaces. The main challenge in pursuing integrated devices capable of simultaneously generating indistinguishable single photons and multi-dimensionally engineering their optical states is the intrinsic incompatibility between the relatively sharp cavity resonances for enhancing light-matter interactions and the broadband metasurfaces for manipulating optical states. In addition, flying qubits featuring topological textures could potentially provide advantages such as robust light propagation and high-density storage. Achieving all the crucial ingredients, including source performance (brightness, single-photon purity and photon indistinguishability), mode characteristics (directionality, polarization, OAM) and topological spin textures within a universal platform is highly desirable yet technologically formidable.

In this work, we experimentally demonstrate monolithic microcavity-metalens interfaces uniquely combining the advantages of large Purcell enhancements enabled by the cavity QED effect and flexible optical state manipulation empowered by metasurfaces. Due to the unique configuration of the microcavity-metalens interface, we have successfully matched the mode profiles between the 2- $\mu\text{m}$ -diameter output of the micropillar and the 200- $\mu\text{m}$ -diameter metalens, without compromising the cavity performance. Indistinguishable single-photon generation and on-demand photonic state engineering are achieved in an integrated device, exhibiting a multi-photon suppression with a  $g^{(2)}(0) = 0.070(1)$ , a photon extraction efficiency (at the first lens) up to 35.7(5)%, a photon indistinguishability (with a delay of 13 ns) of 0.736(2) and arbitrarily

tailored optical states in radiation divergence, emission directionality, polarization state and orbital angular momentum (OAM). We further demonstrate the on-demand generation of polarization-OAM entanglement with high fidelity. Finally, single photons whose spin states feature various skyrmionic textures are achieved. Such a unique combination of quantum light sources and metalenses fuses the very active research fields of integrated quantum photonics and meta-optics [29,41,42]. The state-of-the-art solid-state quantum light sources equipped with the ability of on-demand photonic state manipulation bring unprecedented opportunities to explore structured light-matter interactions at the nanoscale and high-dimensional integrated photonic quantum technology [43–45].

## 2 Results

### 2.1 Operation principle of monolithic microcavity-metalens interfaces

The monolithic interface consists of a pair of a QD-micropillar single-photon source and an ultra-thin metalens, which are accurately aligned on the front side and back side of an III-V compound semiconductor chip, respectively, as schematically shown in Fig. 1(a). The micropillar and metalens are decoupled in the near-field, enabling independent optimizations of the single-photon generation and the wavefront shaping. A single epitaxially grown InAs QD is positioned in the center of a 3  $\mu\text{m}$ -diameter micropillar with 30 (20) pairs of top (bottom)  $1/4 \lambda$   $\text{Al}_{0.9}\text{Ga}_{0.1}\text{As}/\text{GaAs}$  distributed Bragg reflectors (DBRs), as presented in Fig. 1(b). The high-quality (Q) factor and the wavelength-scale mode volume associated with the micropillar allow the enhanced spontaneous emission rate and improved photon extraction efficiency for the single photons emitted from the QD, as numerically simulated in Fig. 1(c). Due to the higher reflectivity of the top DBR, the single photons emitted from the QD are guided towards the GaAs substrate which is transparent at the emission wavelength, see numerical simulation in Fig. 1(f) and Fig.S1 in Supplementary Materials (SM). The emitted single photons are in a Gaussian-like mode [18,25,46] with a divergence angle of  $8.25^\circ$  at the output of the micropillar, as shown in Fig. 1(g). By propagating through a 350  $\mu\text{m}$ -thickness substrate, the beam diameter expands from  $\sim 2 \mu\text{m}$  to  $\sim 103 \mu\text{m}$ , see Fig. 1(h), which is crucial to achieve mode matching between the microcavity and the metalens for efficient wavefront shaping. On the backside of the chip, a metalens with a diameter of 200  $\mu\text{m}$  is aligned to the emitted single photons for arbitrary phase front engineering. The metalens is composed of cuboid-shaped GaAs meta-atoms, whose height (H), lengths in X (L) and Y (W) directions, periodicities ( $P_x$ ,  $P_y$ ) in X and Y directions, and orientation angle ( $\theta$ ) can be well controlled to achieve a variety of functionalities, as shown in Fig. 1(d) and further elaborated in Fig. S2. Each GaAs meta-atom serves as a truncated rectangular waveguide, being able to introduce desired and independent phase shifts ( $\varphi$ ) to the right-handed circularly polarized (RCP) light and left-handed circularly polarized (LCP) light. The phase from 0 to  $2\pi$  is digitized into 8 pieces by varying L and W with transmissions above 0.6, as shown in Fig. 1(e). The transmission of the meta-atom can be improved by using smaller periodicities ( $P_x$ ,  $P_y$ ) (Fig. S3), which is however technologically challenging. The orientation angle ( $\theta$ ) provides an additional degree of freedom to engineer the Pancharatnam-Berry (PB) phase [47], which is crucial for the decoupling and independent phase control of the RCP and LCP channels.

### 2.2 Fabrication of monolithic microcavity-metalens interfaces

We have developed a highly customized fabrication process to implement our proposed device, as schematically shown in Fig. 2. A planar cavity consisting of 20 pairs of bottom  $1/4 \lambda$   $\text{Al}_{0.9}\text{Ga}_{0.1}\text{As}/\text{GaAs}$  DBR, a  $\lambda$  GaAs cavity containing single InAs QDs and 30 pairs of top  $1/4 \lambda$   $\text{Al}_{0.9}\text{Ga}_{0.1}\text{As}/\text{GaAs}$  DBR is grown on a  $350 \mu\text{m}$  double-side polished GaAs substrate via molecule beam epitaxy. Two sets of metallic marks which are used for positioning QDs in the micropillar and aligning metalens to the micropillar are fabricated on the front side of the wafer by using an electron-beam lithography (EBL) and a lift-off process (Fig. 2(a)). A double-sided photolithography and a lift-off process are used to create alignment marks on the backside of the chip (Fig. 2(b)). The alignment accuracy between the front side marks and back side marks is within  $1 \mu\text{m}$  (see Methods and Fig. S4), ensuring that all the emitted single photons can be modulated by the metalens. The spatial positions of individual QDs respective to the front alignment marks are extracted by using our well-established fluorescence imaging technique (Fig. 2(c)) [48,49]. Deterministically coupled QD-micropillar single-photon sources are realized by using a second aligned EBL and a chlorine-based dry etching (Fig. 2(d)). The front side of the chip is then planarized with SU-8 photoresist to protect the micropillars in the following metalens fabrication process (Fig. 2(e)). Finally, metalenses are fabricated on the back side of the chip via the third aligned EBL and a dry etching process (Fig. 2(f)). The scanning electron microscope (SEM) images with different magnifications of a fabricated micropillar and a metalens are presented in Fig. 2(g,h). We systematically optimized the EBL exposure parameters and dry etching recipes for micropillars and metalenses individually, leading to high-quality fabrication with vertical etching profiles and excellent surface smoothness.

### 2.3 Bright and indistinguishable single-photon emissions from micropillar-metalens interfaces

In the experiment, we first examine the characteristics of the emitted single photons whose emission divergence angle is squeezed by using a collimation metalens, as schematically shown in Fig. 3(a). The optical characterization setup is shown in Fig. S6. The micro-photoluminescence ( $\mu\text{PL}$ ) spectra of the micropillar-metalens system under non-resonant excitation are presented in Fig. 3(b). A Q-factor of 2823 is extracted for the investigated micropillar cavity by fitting the high-power cavity spectrum (the broad peak) with a Lorentzian function. Very sharp emission lines (narrow peaks) associated with single QDs are clearly observed at low excitation powers. Detuning between the QDs and the cavity mode can be controlled by varying the system's temperature. The far-field radiation of QD emission after the metalens is measured by using an angle-resolved spectroscopy (see details in Fig. S6), exhibiting a beam divergence angle much smaller than that of a reference device without passing any collimation metalens, as shown in Fig. 3(c,d). The X-cut and Y-cut of the far-field patterns in Fig. 3(c,d) are presented in Fig. 3(e), revealing a beam divergence angle of  $1.44^\circ$  ( $1.06^\circ$ ) and  $28.30^\circ$  ( $25.22^\circ$ ) in X(Y) direction for the collimated and uncollimated quantum emission, respectively. In Fig. 3(f), time-resolved measurements of the QD (a negatively charged exciton) under on-resonance and off-resonance conditions reveal an appreciable reduction of the lifetime from  $675.6(7)$  ps to  $205.5(2)$  ps, which corresponds to a spontaneous emission rate enhancement by a factor of  $\sim 3.288(5)$ . The deviation of the measured Purcell factor from the calculated value of 5.37 by using a measured Q-factor of 2830(1) (see details in Fig. S7) is probably because of the reduced accuracy in positioning process in which both QDs and the alignment marks are imaged through a  $350 \mu\text{m}$  substrate. We further perform pulsed resonant excitation on the investigated single QD under the transmission configuration. A clear Rabi oscillation behavior as a function

of the excitation power (Fig. 3(g)) is observed, which is consistent with the coherent nature of a two-level quantum system. The brightness of the source is evaluated from the measured single-photon count rate of 595 kHz in the avalanche photodiode (APD) at  $\pi$ -pulse and the calibrated setup transmission, resulting in an extraction efficiency of 35.7(5)% at the first collection lens (see details in Tab. S1). We note that this value already includes the loss induced by the metalens. On the other hand, the single-photon purity and the photon indistinguishability mainly relate to the excitation method and the charge environment of the QDs, which are not expected to decrease with the implementation of the metalens. The coupling efficiency of the emitted single photons into a single-mode fiber is  $\sim 0.65$  by using the free space path as a reference, which is competitive to the state-of-the-art [50,51]. The indistinguishability of the emitted single photons at  $\pi$ -pulse is measured by using Hanbury-Brown-Twiss and Hong-Ou-Mandel interferometers, giving rise to a multi-photon suppression of a  $g^{(2)}(0) = 0.070(1)$  and photon indistinguishability with a visibility of  $V_{\text{HOM}} = 0.736(2)$  respectively, as presented in Fig. 3(h,i). The measured indistinguishability is still lower than the state-of-the-art of microcavity-based single-photon sources [18,19,22,23,25], but serves as the first report for quantum radiation from single quantum emitters integrated with metasurfaces.

## 2.4 Tailoring quantum emissions in multiple degrees of freedom

After carefully characterizing the collimated single photons emitted from the micropillar-metalens interface, we introduce more complex functionalities to the metalens for the multi-dimensional engineering of quantum emissions. We design a representative metalens with distinct functionalities and increasing complexity. This multi-functional device simultaneously focuses and deflects RCP and LCP single photons in different directions, and the single photons at each direction are encoded with different helical phase fronts carrying distinctive OAMs. Considering that the fundamental mode of the micropillar is near-Gaussian [52], the performance of the metalens is numerically simulated by passing a Gaussian beam, which mimics the single photons coupled to the cavity mode, across the designed phase profiles, as presented in Fig. 4(a). The detailed design procedure and the corresponding phase profiles for achieving these designed functionalities are presented in Fig. S8. The experimental verification of the proposed device functionality is presented in Fig. 4(b). The RCP and LCP single photons with different values are focused and deflected to the targeted directions, which is in excellent agreement with Fig. 4(a). We employ a simplified method to characterize the emitted quantum optical vortices by using offset interference patterns, which was successfully demonstrated in a recent work [40]. The topological numbers of the structured single photons are quantitatively extracted with  $L_{\text{RCP}} = -1$  and  $L_{\text{LCP}} = 3$  in Fig 4(b), which faithfully produces the results in the numerical simulations as presented in Fig. 4(a). To further evaluate the purity of the OAM states, we performed projection measurements by passing the emitted single photons from the RCP and LCP channels through a series of vortex wave plates (VWPs) with varying topological charges  $l$ , as illustrated in Fig. 4(c,d), respectively. The corresponding OAM mode spectra, presented in Fig. 4(e,f), were obtained from these projection results. The OAM purities of 82.2(2)% and 72.0(4)% are extracted for  $L_{\text{RCP}} = -1$  and  $L_{\text{LCP}} = 3$  (see Methods), respectively. As a result, our micropillar-metalens interfaces convincingly demonstrate full and independent control of bright and indistinguishable single photons in radiation divergence, emission directionality, polarization state and OAM dimensions, simultaneously.

## 2.5 Generation of polarization-OAM entanglement in single photons

We further demonstrate the generation of quantum entanglement between the polarization state and the OAM of the single photons by using the micropillar-metalens interface. Under LA-phonon-assisted excitation [53,54], we can generate a stream of horizontally polarized single photons without OAM, denoted as  $|H, 0\rangle$ , as shown in Fig. 5(a). These photons pass a metalens acting as a q-plate with  $q = 1/2$ , resulting in the formation of vectorial single photons with non-uniform polarization and intensity distributions, as shown in Fig. 5(b). In such a state, polarization state and OAM are entangled in the form of Bell state  $|\Phi_+\rangle = 1/\sqrt{2}(|L, -1\rangle + |R, +1\rangle)$  [38,55], as schematically illustrated in Fig. 5(a). The maximally entangled Bell state with an entanglement fidelity of  $F = 0.8914 \pm 0.0023$  is experimentally measured by using quantum state tomography (QST) (see the QST setup in Fig. S6, the projection states in Fig. S9 and the detailed description in Methods) and reconstructed via a maximum likelihood estimation method [56]. The retrieved density matrix is shown in Fig. 5(c,d), which is in excellent agreement with the theoretical values in Fig. 5(e,f).

## 2.6 Creation of single photons with local topological spin textures

Finally, we present the versatile creations of quantum emission with local topological spin textures, namely single-photon skyrmions, by using our devices. It has been very recently shown that the non-local correlations between polarization and OAM associated with a photon pair can be exploited as a resilient resource of quantum entanglement [57]. On the other hand, the quantum state of light carrying local skyrmionic texture is highly desirable due to the applications in high-capacity quantum communication and high-density quantum memory, yet their on-chip implementation is still elusive [58,59]. Single-photon skyrmions have been very recently generated in a solid-state cavity quantum electrodynamics system under a strong magnetic field [60]; however, such a device is only capable of producing very specific optical skyrmions with a fixed topological charge, without revealing the advantages of such topologically structured light. Optical skyrmions with local topologies can be synthesized via the superposition of two light beams with orthogonal circular polarizations and different OAM orders [61–63]. As schematically shown in Fig. 6(a), the horizontally polarized single photons with zero OAM pass through the metalens, encoding a helical phase front to the LCP component. The created polarization state features a topological texture in the form of an optical skyrmion, which can be written as  $|\Psi_s\rangle = 1/\sqrt{2}(|R, 0\rangle + |L, -s\rangle)$ , where the skyrmion number  $s$  equals to the OAM value of the LCP component. We experimentally generate optical skyrmions with skyrmion numbers equal to 1, as shown in Fig. 6(b). Within the cross-section of the optical beam, the polarization vector flips upward while swirling, and all the polarization states represented by the unit Poincaré sphere are experienced, thus fulfilling the skyrmion topology. From the measured Stokes vectors, skyrmion numbers of 0.99 are extracted (see Methods), which are very close to theoretical values of 1. To further demonstrate the functionality of our microcavity-metalens interfaces, we generate optical skyrmions with skyrmion numbers ranging from 2 to 5, as shown in Fig. S10. One of the greatest promises of topologically structured light is to provide robust propagation against disorders [64], which has recently stimulated great interests in the stability of optical skyrmions [65–67]. The propagation of single-photon skyrmions in an atmospheric turbulence can be numerically simulated, as shown for one example in Fig. 6(c). Despite local changes in the spin textures, the skyrmion number is slightly reduced from an ideal value of 1.00 down to 0.98 under a turbulence strength with ratio  $D/r_0 = 0.5$  (see Methods). The simulation is experimentally verified by examining the skyrmion numbers of the single-photon

skyrmions propagating through artificial atmospheric turbulences with different strengths, which are created by a spatial phase modulator (SLM) [68,69], see more details in Methods. While local variations are observed in the Stokes parameters and the skyrmion boundaries, the skyrmion number remains stable under different strengths of perturbation, as shown in Fig. 6(d), suggesting a resilient propagation related to the topology. For comparison, we also test propagation of single photons carrying OAM (RCP channel of Fig. 4(b)) through the same atmospheric turbulences. Single photons with skyrmionic textures exhibit greater robustness against atmospheric turbulence than those carrying OAM with the same topological charge. The statistical measurements (represented by the error bars), based on 50 realizations for each strength of the turbulence, are shown in Fig. 6(e). The local topologies carried by single-photon skyrmions could potentially provide an unparalleled opportunity to access resilient quantum technology such as robust quantum entanglement generations [44], high-dimensional quantum communications [43,45] and high-capacity quantum memories [70].

### 3. Discussions

We have successfully demonstrated monolithic microcavity-metalens interfaces capable of generating indistinguishable quantum emission and simultaneously manipulating their optical states in multiple physical degrees of freedom. The cQED effect associated with the micropillar enables single-photon emission with simultaneous high degrees of source brightness, single-photon purity and photon indistinguishability while the metalenses endow the ability to independently manipulate the quantum emission in radiation divergence, emission directionality, polarization state and OAM dimension. The polarization-OAM entanglement and single-photon skyrmions are successfully created in our monolithic devices. The all-in-one functionalities in a single chip offer unique advantages in terms of device footprint, operation stability, and scalability, placing our device as a record-performance source among the existing high-dimensional single-photon sources based on quantum emitters integrated with metasurfaces, see Tab. S2 in SM. Our devices are particularly appealing to the pursuit of a quantum network with larger information capacity, resilience to noise and improved security [71]. From a view of fundamental physics, the investigation of structured light-matter interactions down to the single quanta level may bring new insight into chiral quantum emission [72] and spin-photon quantum interfaces [54,73]. Our work bridges the research field of quantum photonics and meta-optics, opening up an avenue toward high-dimensional multi-photon experiments in which device scalability and system efficiency play an essential role.

## 4. Methods

### 4.1 Epitaxial growth and fabrication yield

A double-sided polished III-V wafer that consisted of a single layer of low-density In (Ga) As QDs between 30 (top) and 20 (bottom) GaAs/Al<sub>0.9</sub>Ga<sub>0.1</sub>As DBRs is grown via molecular beam epitaxy. The InAs/GaAs QDs were grown using a high-temperature, ultra-low-rate growth method combined with the indium flush technique. A substrate temperature of 530 °C and an InAs deposition rate of 0.002 ML/s were used to achieve ultra-low dot densities. To tune the emission wavelength and improve size uniformity, a 6 nm low-temperature GaAs cap was deposited, followed by a thermal annealing step under As flux to partially desorb indium. During

QD deposition, substrate rotation was stopped to introduce a lateral gradient in InAs coverage, enabling post-growth selection of regions with suitable QD densities. We choose an area with a QD density  $\sim 0.01/\mu\text{m}^2$  for making QD-micropillar single-photon sources. The Q-factors of the fabricated micropillars range from 1750 to 3300. The planar cavity is etched into 3  $\mu\text{m}$ -diameter micropillars with QDs embedded in the center. For 20% of the fabricated devices, we can find single QDs whose excitonic transitions are spectrally in the vicinity of the cavity modes. We note this value can be significantly improved in our future devices by either implementing the spectral imaging technique [49] or using in-situ strain tuning technology [74], both of which have recently been demonstrated in the QD-micropillar system.

The alignment of the micropillars to the metalenses is achieved using alignment markers on both the front side and back side of the sample. After fabricating the frontside alignment markers (Fig. 2(a)), we flipped the sample and fabricated the backside alignment markers. The alignment procedure for the backside pattern was done in a standard double-sided mask aligner (EVG 620). The whole procedure is as follows: First a photo of the marker on the mask is taken using the backside microscope. Then, the chip is inserted frontside-down to the equipment, where the patterns, including alignment markers, on the front side of the chip are facing down to the backside microscope (as shown in Fig. 2(b)). Subsequently, the chip is aligned to the photo of the mask marker taken in the first step with the help of the backside microscope. When aligned, exposure is performed on the backside of the chip, which is now facing up to the mask. This method does not rely on imaging through the GaAs substrate, thereby avoiding image distortion and ensuring an alignment accuracy within 1  $\mu\text{m}$  (see details in SM). Our numerical simulations (see Fig. S5) show that such a small alignment offset has negligible influence on the device performances.

Considering that the conventional QD positioning methods based on fluorescence imaging in reflection configuration are not applicable in our experiment, we developed a transmission-mode fluorescence imaging technique for QD positioning. As shown in Fig. S6, the sample is mounted in a transmission-mode closed-cycle cryostat, allowing efficient excitation from the front side and collection of the emitted photons from the backside. Meanwhile, we illuminate the frontside alignment markers using a 1050 nm LED and obtain the markers image via reflection imaging, which is shown in Fig. 2(c). Finally, the position of QDs is accurately determined by combining the fluorescence imaging of QDs with the reflected imaging of the frontside alignment markers. In the fabrication process, the deterministically coupled QD-micropillars are realized by an aligned EBL using the frontside alignment markers and the metalenses are fabricated via an aligned EBL based on the backside alignment markers, as illustrated in Fig. 2(d) and (f). The alignment accuracy within 1  $\mu\text{m}$  between the frontside markers and back-side markers ensures the alignment of QDs to the micropillars, and the micropillars to the metalenses.

## 4.2 Design of multifunctional metalens

To design the multi-functional metalens in our microcavity-metalens interfaces, we first optimize the size of meta-atoms. The height (H) and the period (P) of the meta-atoms are fixed (H = 900 nm, P = 400 nm), considering the possibility and difficulty of fabrication. Phase retardance (Fig. S2(a) and Fig. S2(b)) and transmission coefficients (Fig. S2(d) and Fig. S2(e)) of the meta-atoms with different sizes for an emission wavelength of 920 nm in X-polarization and Y-polarization are calculated. To achieve the function of metalens that enables to manipulation of quantum emission in two orthogonal circular polarizations (RCP and LCP), the meta-atoms

serve as nano half-waveplates. Hence, only the parameters that the phase difference between X-polarization and Y-polarization is equal to  $\pi$  are considered, which are highlighted by the blue circles in Fig. S2(c). Taking the transmission efficiency into account, we finally select 8 meta-atoms that perform 8 phase steps between  $0-2\pi$  as shown in Fig. S2(f). Secondly, we decide the distribution of the meta-atoms according to the tailoring functions required. The basic process is illustrated in Fig. S8. We calculate two separate phase maps for the RCP and LCP channels (Fig. S8(a)). To achieve the complex functions of the metalens including beam focusing, beam deflecting and OAM encoding, the phase profile in each channel contains a collimator phase, a deflector phase and an OAM phase (Fig. S8(a)). Next, the phase shift ( $\varphi_x$ ) and the orientation ( $\theta$ ) of the meta-atoms are calculated from the phase profiles of RCP and LCP (Fig. S8(b)). The lengths of meta-atoms in X direction (L) and Y direction (W) are thus decided by the required phase shift, according to the optimal design of the parameters of meta-atoms as listed in Fig. S2(f). Then the phase profiles in RCP and LCP channels are thus transferred to the actual distribution of metalens (Fig. S8(b)). We note that the higher-order diffractions can be safely neglected in our experiments due to their weak intensities and large emission angles beyond the numerical aperture of the objective (see Fig. S11 in SM).

### 4.3 Optical characterizations

The schematic of the setups for optical characterization is presented in Fig. S6. The microcavity-metalens interfaces are located in a closedcycle cryostat with a base temperature of 5.8 K. The QDs embedded in the micropillar can be excited from the front side by continuous wave (CW) or pulsed lasers via a  $\times 20$  objective with a numerical aperture of 0.40. The downward emitted photons tailored by metalens are collected in transmission geometry by a  $\times 50$  objective with a numerical aperture of 0.65. A 1050 nm LED coupled to the main optical path with dichroic mirrors (DM) is used to illuminate the marks on both sides of the chip. The micro-photoluminescence ( $\mu$ PL) spectra of the micropillar-metalens system can be easily obtained under non-resonant conditions by a 785 nm CW laser (Fig. 3(b)). To further characterize the emitted single photons from the micropillar-metalens interfaces, the QD is resonantly excited using a pulsed laser with a repetition of 79.6 MHz in a cross-polarization configuration. Collected by optical fiber, the emitted single photons are sent to a monochromator for the spectral analysis or to avalanche photodiodes (APDs) for lifetime characterizations (Fig. 3(f)), HanburyBrown-Twiss (HBT) measurements (Fig. 3(h)) and Hong-Ou-Mandel (HOM) measurements (Fig. 3(i)). To characterize the multidimensional quantum emission engineered by integrated metalens (Fig. 4(b)), a Fourier transform lens is flipped into the optical path and maps the far-field plane to an electron-multiplying charge-coupled device (EMCCD). By inserting vortex waveplates (VWPs) with different topological charge in the imaging arm of the setup, we can measure the OAM mode spectrum of the emitted photons. The mode components of each order can be extracted by calculating the intensity of the central area of the projection pattern, which is defined by the diameter of the converted Gaussian pattern. A quantum state tomography (QST) setup consisting of a VWP and a series of QWP, HWP and polarizer is used to verify the polarization-OAM entanglement of the single photons shown in Fig. 5(a). To perform full QST on the state, 16 sets of measurements are required, which is illustrated in Fig. S9. From the 16 measured projection intensities, we reconstructed the density matrix of the state using a maximum likelihood estimation method [56], as presented in Fig. 5(c,d).

#### 4.4 Topologies of skyrmions

The topological properties of the optical quantum skyrmions can be characterized by the skyrmion number, which is defined as [75,76]

$$s = \frac{1}{4\pi} \iint_{\sigma} \mathbf{n} \cdot \left( \frac{\partial \mathbf{n}}{\partial x} \times \frac{\partial \mathbf{n}}{\partial y} \right) dx dy ,$$

where  $\mathbf{n}(x,y)$  represents the Stokes vectors to construct a skyrmion and  $\sigma$  denotes the skyrmion area. By mapping the vector fields on a unit Poincaré sphere, the vectors can be written as  $\mathbf{n} = (\cos\alpha(\theta)\sin\beta(r), \sin\alpha(\theta)\sin\beta(r), \cos\beta(r))$ , then the skyrmion number can be separated into two integers:

$$\begin{aligned} s &= \frac{1}{4\pi} \int_0^{r_\sigma} dr \int_0^{2\pi} d\theta \frac{d\beta(r)}{dr} \frac{d\alpha(\theta)}{d\theta} \sin\beta(r) \\ &= \frac{1}{4\pi} [\cos\beta(r)] \Big|_{r=0}^{r=r_\sigma} [\alpha(\theta)] \Big|_{\theta=0}^{\theta=2\pi} = q \cdot m , \end{aligned}$$

where the polarity  $q$  is half of the difference in the out-of-plane component between the center and boundary of the skyrmionic vector field, and the vorticity  $m$  controls the helical distribution of the in-plane component. For the skyrmions state  $|\Psi_s\rangle = 1/\sqrt{2}(|R, 0\rangle + |L, -s\rangle)$  in our experiment,  $q$  equals to 1 (spin-down arrow at the center and spin-up arrow at the edge) and  $m$  is given by the difference of the OAM value between the RCP and LCP light, which is  $s$ , thus the theoretical skyrmion number is  $s$ . For the experimentally measured Stokes fields, we applied linear interpolation followed by a Gaussian filter as part of the post-processing procedure to suppress noise and enhance the accuracy of the skyrmion number calculation. Besides, due to the different sizes of the skyrmionic Stokes fields, careful area selection was crucial.

#### 4.5 Simulation and experiment of single-photon skyrmion propagation in the presence of atmospheric turbulence

There are multiple approaches to introduce turbulence into an optical system, such as the von Kármán [77] and Kolmogorov [78] phase screens, which are some of the more commonly employed models. For the study of optical skyrmions, Kolmogorov phase screens are more ideal since they offer computational efficiency while providing an accurate representation of atmospheric turbulence. By applying a Kolmogorov phase screen, one generates a phase mask that only distorts the phase of the wavefront, without altering the beam's intensity. However, in the far-field, this phase disturbance manifests as distortions in phase, intensity and polarization. This facilitates the study of how turbulence-induced distortions affect the formation of skyrmions and their corresponding topological charge. The phase structure function in Kolmogorov turbulence can be given by [79,80]

$$\Phi(\rho) = 6.88 \left( \frac{D}{r_0} \right)^{5/3} \left( \rho \sin \frac{\phi}{2} \right)^{5/3} ,$$

where the Fried parameter  $r_0$  is a metric of the transmission quality after the propagation through a turbulent medium and  $D$  is the diameter of the section of the atmosphere. Traditionally, the Fried parameter is mathematically defined as  $r_0 = [0.423k^2 \int C_n^2 z' dz']^{-3/5}$ , where  $k = 2\pi/\lambda$  is the optical wavenumber, and  $C_n^2$  is the refractive index structure constant which determines the strength of atmospheric turbulence. In our work, we characterize the turbulence strength by the ratio  $D/r_0$ .

By the Fraunhofer diffraction integral with a Fourier transform algorithm [81], we can numerically obtain the Stokes skyrmion textures after propagation through atmospheric turbulence (Fig. 6(c)).

#### 4.6 Skyrmion boundary retrieval in the presence of atmospheric turbulence

In the absence of turbulence, the Stokes skyrmion is well-defined with clear circular symmetry, allowing the topological charge to be determined by integrating over a circular contour. However, turbulence disrupts this symmetry and a circular integral no longer gives us the correct topological charge. Therefore, it is necessary to accurately define an adaptive contour that accurately captures the topological charge. Here, we applied the Active Contour Model (ACM), otherwise known as Snakes [82]. Snakes are an unparalleled tool widely employed in computer vision, primarily used to outline an object’s boundary in a noisy two-dimensional environment. They are adaptive, energy-minimizing contours that evolve iteratively under the influence of internal and external forces, denoted by  $E_{int}$  and  $E_{ext}$ , respectively. Mathematically, the Snake’s energy function is given by

$$E_{snake} = \int_0^1 (E_{int} + E_{ext}) ds ,$$

where  $ds$  represents the differential element of the curve parameter. The optimization of the snake function is based on the concept of gradient descent. Starting from an initial contour, the algorithm iteratively minimizes the Snake function’s energy, moving in the direction of the negative gradient at each step. This process continues until the local minima are found, at which point the contour outlines the boundary of the image. As we can see in Fig. 6(c), with the assistance of Snakes, we can accurately track the skyrmion boundary of the deformed Stokes skyrmion textures and recover the skyrmion number, which is consistent with the undisturbed one. In the experiment, the atmospheric turbulence with different turbulence strengths is introduced by a spatial light modulation (SLM) displaying a Kolmogorov phase pattern with different ratios  $D/r_0$ . We measure the Stokes parameters of the single-photon skyrmions reflected by the SLM and reconstruct the Stokes vector fields. Assisted by the boundary identification algorithm Snakes, the recovered skyrmion number remains stable under different strengths of perturbation (shown in Fig. 6(d)), suggesting a resilient propagation related to the topology.

**Acknowledgements.** This research was supported by the National Key Research and Development Program of China (2021YFA1400800); National Natural Science Foundation of China (62035017, 12361141824, 12304409); Natural Science Foundation of Guangdong Province (2023B1515120070); Guangdong Provincial Quantum Science Strategic Initiative (GDZX2206001, GDZX2306003); Singapore Ministry of Education (MOE) AcRF Tier 1 grants (RG157/23 & RT11/23); Singapore Agency for Science, Technology and Research (A\*STAR) MTC Individual Research Grants (M24N7c0080) and the National Super-Computer Center in Guangzhou.

**Competing interests.** The authors declare no conflict of interest.

**Availability of data and materials.** The data that support the findings of this study are available within the paper and the supplementary material. Other relevant data are available from the corresponding authors on reasonable request.

**Author Contributions.** J. L. conceived the project; S. F. L., J. L., and H. Q. L. designed the epitaxial structure; H. Q. L. and H. Q. N. grew the quantum dot wafers; J. T. M., S. F. L., B. C., G. X. Q. N. M-C, and D. Z. W. developed the theory model and designed the devices; D. L., J. T. M., S. F. L., J. W. Y., K. X. C., and X. S. L. fabricated the devices; J. T. M. and S. F. L. built the setup and performed the optical measurements; J. T. M., Y. J. S. and J. L. analyzed the data; J. L. and J. T. M. prepared the manuscript with inputs from all authors, Z. C. N. Y. Y., Y. J. S., L. L., X. H. W. and J. L. supervised the project.

## References

- [1] O'Brien, J. L., Furusawa, A. & Vučković, J. Photonic quantum technologies. *Nat. Photon.* **3**, 687-695 (2009).
- [2] Gisin, N. & Thew, R. Quantum communication. *Nat. photon.* **1**, 165-171 (2007).
- [3] O'Brien, J. L. Optical quantum computing. *Science* **318**, 1567-1570 (2007).
- [4] Zhong, H.-S. et al. Quantum computational advantage using photons. *Science* **370**, 1460-1463 (2020).
- [5] Madsen, L. S. et al. Quantum computational advantage with a programmable photonic processor. *Nature* **606**, 75-81 (2022).
- [6] Giovannetti, V., Lloyd, S. & Maccone, L. Advances in quantum metrology. *Nat. Photon.* **5**, 222-229 (2011).
- [7] McKeever, J. et al. Deterministic generation of single photons from one atom trapped in a cavity. *Science* **303**, 1992-1994 (2004).
- [8] Keller, M., Lange, B., Hayasaka, K., Lange, W. & Walther, H. Continuous generation of single photons with controlled waveform in an ion-trap cavity system. *Nature* **431**, 1075-1078 (2004).
- [9] Aharonovich, I., Englund, D. & Toth, M. Solid-state single-photon emitters. *Nat. Photon.* **10**, 631-641 (2016).
- [10] Michler, P. Quantum dots for quantum information technologies, vol. 237 (Springer, 2017).
- [11] Senellart, P., Solomon, G. & White, A. High-performance semiconductor quantum-dot single-photon sources. *Nat. Nanotechnol.* **12**, 1026-1039 (2017).
- [12] Zhou, X., Zhai, L. & Liu, J. Epitaxial quantum dots: a semiconductor launchpad for photonic quantum technologies. *Photon. Insights* **1**, R07-R07 (2023).
- [13] Castelletto, S. et al. A silicon carbide room-temperature single-photon source. *Nat. Mater.* **13**, 151-156 (2014).
- [14] Zhou, Y. et al. Room temperature solid-state quantum emitters in the telecom range. *Sci. Adv.* **4**, eaar3580 (2018).
- [15] Montblanch, A. R.-P., Barbone, M., Aharonovich, I., Atatüre, M. & Ferrari, A. C. Layered materials as a platform for quantum technologies. *Nat. Nanotechnol.* **18**, 555-571 (2023).
- [16] Wang, J., Sciarrino, F., Laing, A. & Thompson, M. G. Integrated photonic quantum technologies. *Nat. Photon.* **14**, 273-284 (2020).
- [17] Elshaari, A. W., Pernice, W., Srinivasan, K., Benson, O. & Zwiller, V. Hybrid integrated quantum photonic circuits. *Nat. Photon.* **14**, 285-298 (2020).
- [18] Somaschi, N. et al. Near-optimal single-photon sources in the solid state. *Nat. Photon.* **10**, 340-345 (2016).
- [19] He, Y.-M. et al. Deterministic implementation of a bright, ondemand single-photon source with near-unity indistinguishability via quantum dot imaging. *Optica* **4**, 802-808 (2017).
- [20] Wang, H. et al. Towards optimal single-photon sources from polarized microcavities. *Nat. Photon.* **13**, 770-775 (2019).

- [21] Liu, J. et al. A solid-state source of strongly entangled photon pairs with high brightness and indistinguishability. *Nat. Nanotechnol.* **14**, 586-593 (2019).
- [22] Wang, H. et al. On-demand semiconductor source of entangled photons which simultaneously has high fidelity, efficiency, and indistinguishability. *Phys. Rev. Lett.* **122**, 113602 (2019).
- [23] Uppu, R. et al. Scalable integrated single-photon source. *Sci. Adv.* **6**, eabc8268 (2020).
- [24] Tomm, N. et al. A bright and fast source of coherent single photons. *Nat. Nanotechnol.* **16**, 399-403 (2021).
- [25] Wei, Y. et al. Tailoring solid-state single-photon sources with stimulated emissions. *Nat. Nanotechnol.* **17**, 470-476 (2022).
- [26] Gazzano, O. et al. Bright solid-state sources of indistinguishable single photons. *Nat. Commun.* **4**, 1425 (2013).
- [27] Yang, J. et al. Tunable quantum dots in monolithic fabry-perot microcavities for high-performance single-photon sources. *Light Sci. Appl.* **13**, 33 (2024).
- [28] Kan, Y. & Bozhevolnyi, S. I. Advances in metaphotonics empowered single photon emission. *Advanced Optical Materials* **11**, 2202759 (2023).
- [29] Ma, J. et al. Engineering quantum light sources with flat optics. *Adv. Mater.* **36**, 2313589 (2024).
- [30] Chen, H.-T., Taylor, A. J. & Yu, N. A review of metasurfaces: physics and applications. *Rep. Prog. Phys.* **79**, 076401 (2016).
- [31] Chen, W. T., Zhu, A. Y. & Capasso, F. Flat optics with dispersionengineered metasurfaces. *Nat. Rev. Mater.* **5**, 604-620 (2020).
- [32] Li, L. et al. Metalens-array-based high-dimensional and multi-photon quantum source. *Science* **368**, 1487-1490 (2020).
- [33] Huang, T.-Y. et al. A monolithic immersion metalens for imaging solid-state quantum emitters. *Nat. Commun.* **10**, 2392 (2019).
- [34] Wu, C. et al. Room-temperature on-chip orbital angular momentum single-photon sources. *Sci. Adv.* **8**, eabk3075 (2022).
- [35] Bao, Y. et al. On-demand spin-state manipulation of single-photon emission from quantum dot integrated with metasurface. *Sci. Adv.* **6**, eaba8761 (2020).
- [36] Komisar, D. et al. Multiple channelling single-photon emission with scattering holography designed metasurfaces. *Nat. Commun.* **14**, 6253 (2023).
- [37] Jia, S. et al. Multichannel single-photon emissions with on-demand momentums by using anisotropic quantum metasurfaces. *Advanced Materials* **35**, 2212244 (2023).
- [38] Stav, T. et al. Quantum entanglement of the spin and orbital angular momentum of photons using metamaterials. *Science* **361**, 1101-1104 (2018).
- [39] Wang, K. et al. Quantum metasurface for multiphoton interference and state reconstruction. *Science* **361**, 1104-1108 (2018).
- [40] Li, C. et al. Arbitrarily structured quantum emission with a multifunctional metalens. *Elight* **3**, 19 (2023).
- [41] Solntsev, A. S., Agarwal, G. S. & Kivshar, Y. S. Metasurfaces for quantum photonics. *Nat. Photon.* **15**, 327-336 (2021).
- [42] Ding, F. & Bozhevolnyi, S. I. Advances in quantum meta-optics. *Mater. Today* (2023).
- [43] Wang, X.-L. et al. Quantum teleportation of multiple degrees of freedom of a single photon. *Nature* **518**, 516-519 (2015).
- [44] Wang, J. et al. Multidimensional quantum entanglement with large-scale integrated optics. *Science* **360**, 285-291 (2018).

- [45] Chen, B. et al. Bright solid-state sources for single photons with orbital angular momentum. *Nat. Nanotechnol.* **16**, 302-307 (2021).
- [46] Ding, X. et al. On-demand single photons with high extraction efficiency and near-unity indistinguishability from a resonantly driven quantum dot in a micropillar. *Phys. Rev. Lett.* **116**, 020401 (2016).
- [47] Berry, M. V. Quantal phase factors accompanying adiabatic changes. *Proc. R. Soc. London. Ser A* **392**, 45-57 (1984).
- [48] Liu, J. et al. Cryogenic photoluminescence imaging system for nanoscale positioning of single quantum emitters. *Rev. Sci. Instrum.* **88**, 023116 (2017).
- [49] Liu, S. et al. Super-resolved snapshot hyperspectral imaging of solid-state quantum emitters for high-throughput integrated quantum technologies. *Nature Photonics* **18**, 967-974 (2024).
- [50] Rickert, L. et al. A fiber-pigtailed quantum dot device generating indistinguishable photons at ghz clock-rates. *Nanophotonics* **14(11)**, 1795-1808 (2025).
- [51] Margaria, N. et al. Efficient fiber-pigtailed source of indistinguishable single photons. arXiv preprint arXiv:2410.07760 (2024).
- [52] Liu, S. et al. Dual-resonance enhanced quantum light-matter interactions in deterministically coupled quantum-dot-micropillars. *Light Sci. Appl.* **10**, 158 (2021).
- [53] Thomas, S. et al. Bright polarized single-photon source based on a linear dipole. *Phys. Rev. Lett.* **126**, 233601 (2021).
- [54] Coste, N. et al. High-rate entanglement between a semiconductor spin and indistinguishable photons. *Nature Photonics* **17**, 582-587 (2023).
- [55] Suprano, A. et al. Orbital angular momentum based intra-and interparticle entangled states generated via a quantum dot source. *Adv. Photon.* **5**, 046008-046008 (2023).
- [56] James, D. F., Kwiat, P. G., Munro, W. J. & White, A. G. Measurement of qubits. *Physical Review A* **64**, 052312 (2001).
- [57] Ornelas, P., Nape, I., de Mello Koch, R. & Forbes, A. Non-local skyrmions as topologically resilient quantum entangled states of light. *Nature Photonics* **18**, 258-266 (2024).
- [58] Shen, Y. et al. Optical skyrmions and other topological quasiparticles of light. *Nature Photonics* **18**, 15-25 (2024).
- [59] Shen, Y., Wang, H. & Fan, S. Free-space topological optical textures: tutorial. *Advances in Optics and Photonics* **17**, 295-374 (2025).
- [60] Ma, J. et al. Nanophotonic quantum skyrmions enabled by semiconductor cavity quantum electrodynamics. *Nature Physics* **21**, 1462-1468 (2025).
- [61] Shen, Y., Martínez, E. C. & Rosales-Guzmán, C. Generation of optical skyrmions with tunable topological textures. *ACS Photonics* **9**, 296-303 (2022).
- [62] Lin, W., Ota, Y., Arakawa, Y. & Iwamoto, S. On-chip optical skyrmionic beam generators. *Optica* **11**, 1588-1594 (2024).
- [63] He, T. et al. Optical skyrmions from metafibers with subwavelength features. *Nature Communications* **15**, 10141 (2024).
- [64] Klug, A., Nape, I. & Forbes, A. The orbital angular momentum of a turbulent atmosphere and its impact on propagating structured light fields. *New Journal of Physics* **23**, 093012 (2021).
- [65] Chen, J., Forbes, A. & Qiu, C.-W. More than just a name? from magnetic to optical skyrmions and the topology of light. *Light: Science & Applications* **14**, 28 (2025).
- [66] He, C., Shen, Y. & Forbes, A. Towards higher-dimensional structured light. *Light: Science & Applications* **11**, 205 (2022).
- [67] Shen, Y., Hou, Y., Papasimakis, N. & Zheludev, N. I. Supertoroidal light pulses as electromagnetic skyrmions propagating in free space. *Nature communications* **12**, 5891 (2021).

- [68] Cox, M. A. et al. Structured light in turbulence. *IEEE Journal of Selected Topics in Quantum Electronics* **27**, 1-21 (2020).
- [69] Toselli, I., Korotkova, O., Xiao, X. & Voelz, D. G. Slmbased laboratory simulations of kolmogorov and non-kolmogorov anisotropic turbulence. *Applied optics* **54**, 4740-4744 (2015).
- [70] Liu, X. et al. Heralded entanglement distribution between two absorptive quantum memories. *Nature* **594**, 41-45 (2021).
- [71] Erhard, M., Krenn, M. & Zeilinger, A. Advances in high-dimensional quantum entanglement. *Nat. Rev. Phys.* **2**, 365-381 (2020).
- [72] Lodahl, P. et al. Chiral quantum optics. *Nature* **541**, 473-480 (2017).
- [73] Cogan, D., Su, Z.-E., Kenneth, O. & Gershoni, D. Deterministic generation of indistinguishable photons in a cluster state. *Nat. Photon.* **17**, 324-329 (2023).
- [74] Chen, Y. et al. In situ three-dimensional strain engineering of solid-state quantum emitters in photonic structures towards scalable quantum networks. *Nature Communications* **16**, 5564 (2025).
- [75] Göbel, B., Mertig, I. & Tretiakov, O. A. Beyond skyrmions: Review and perspectives of alternative magnetic quasiparticles. *Physics Reports* **895**, 1-28 (2021).
- [76] Nagaosa, N. & Tokura, Y. Topological properties and dynamics of magnetic skyrmions. *Nature nanotechnology* **8**, 899-911 (2013).
- [77] Von Karman, T. Progress in the statistical theory of turbulence. *Proceedings of the National Academy of Sciences* **34**, 530-539 (1948).
- [78] Kolmogorov, A. N. The local structure of turbulence in incompressible viscous fluid for very large reynolds. *Numbers. In Dokl. Akad. Nauk SSSR* **30**, 301 (1941).
- [79] Klug, A., Nape, I. & Forbes, A. The orbital angular momentum of a turbulent atmosphere and its impact on propagating structured light fields. *New Journal of Physics* **23**, 093012 (2021).
- [80] Tyler, G. A. & Boyd, R. W. Influence of atmospheric turbulence on the propagation of quantum states of light carrying orbital angular momentum. *Optics letters* **34**, 142-144 (2009).
- [81] Goodman, J. W. Introduction to Fourier optics (Roberts and Company publishers, 2005).
- [82] Kass, M., Witkin, A. & Terzopoulos, D. Snakes: Active contour models. *International journal of computer vision* **1**, 321-331 (1988).

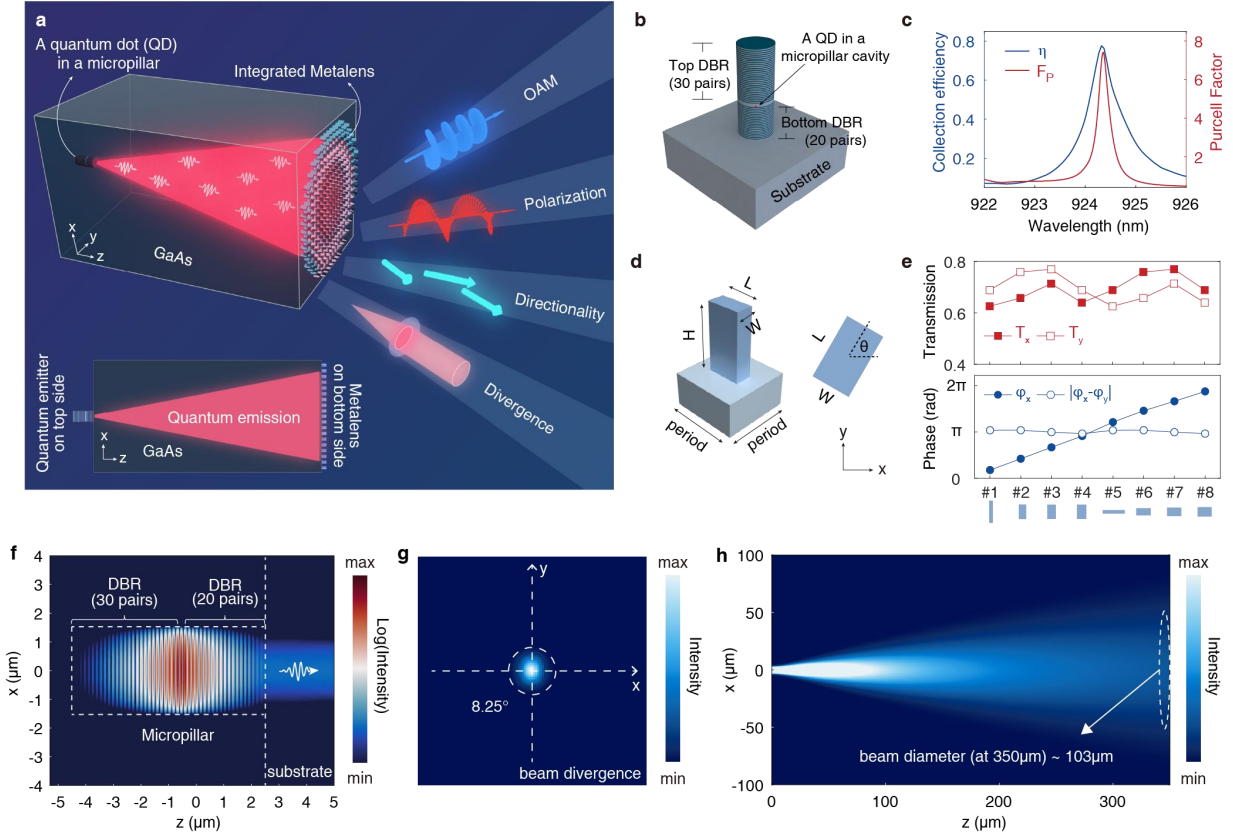


**Fig. 1. Operation principle of the monolithic microcavity-metalens interfaces.** (a) Schematics of the monolithic microcavity-metalens interface. A QD-micropillar single-photon device emits bright and indistinguishable single photons toward its substrate. A metalens on the backside of the chip arbitrarily engineers the photon states of the quantum emission in multiple physical degrees of freedom including radiation divergence, emission directionality, polarization state and OAM. Inset: the XZ plane cross-section of the device. (b) Schematics of the single-photon source on the front side of the chip, consisting of a single QD embedded in the center of a micropillar cavity. The top mirror has 10 more pairs of the DBR than the bottom mirror, which gives rise to the downward photon emission. (c) Numerical simulations of the Purcell factor and the extraction efficiency of the ideal single-photon source. (d) Schematics of the meta-atom acting as a truncated rectangular waveguide to engineer the amplitude and the phase front of the single photons. (e) The calculated transmission and phase shift for meta-atoms with different shapes. (f) Numerical simulation of the single-photon emission to the substrate. (g) Calculated beam divergence of single-photon emission at the output of the micropillar. The DBRs are fully etched in our process. (h) Numerical simulation of the beam propagation of single photons in the substrate. The beam diameter is expanded from  $\sim 2 \mu\text{m}$  to  $\sim 103 \mu\text{m}$  by propagating through a  $350 \mu\text{m}$ -thickness substrate.

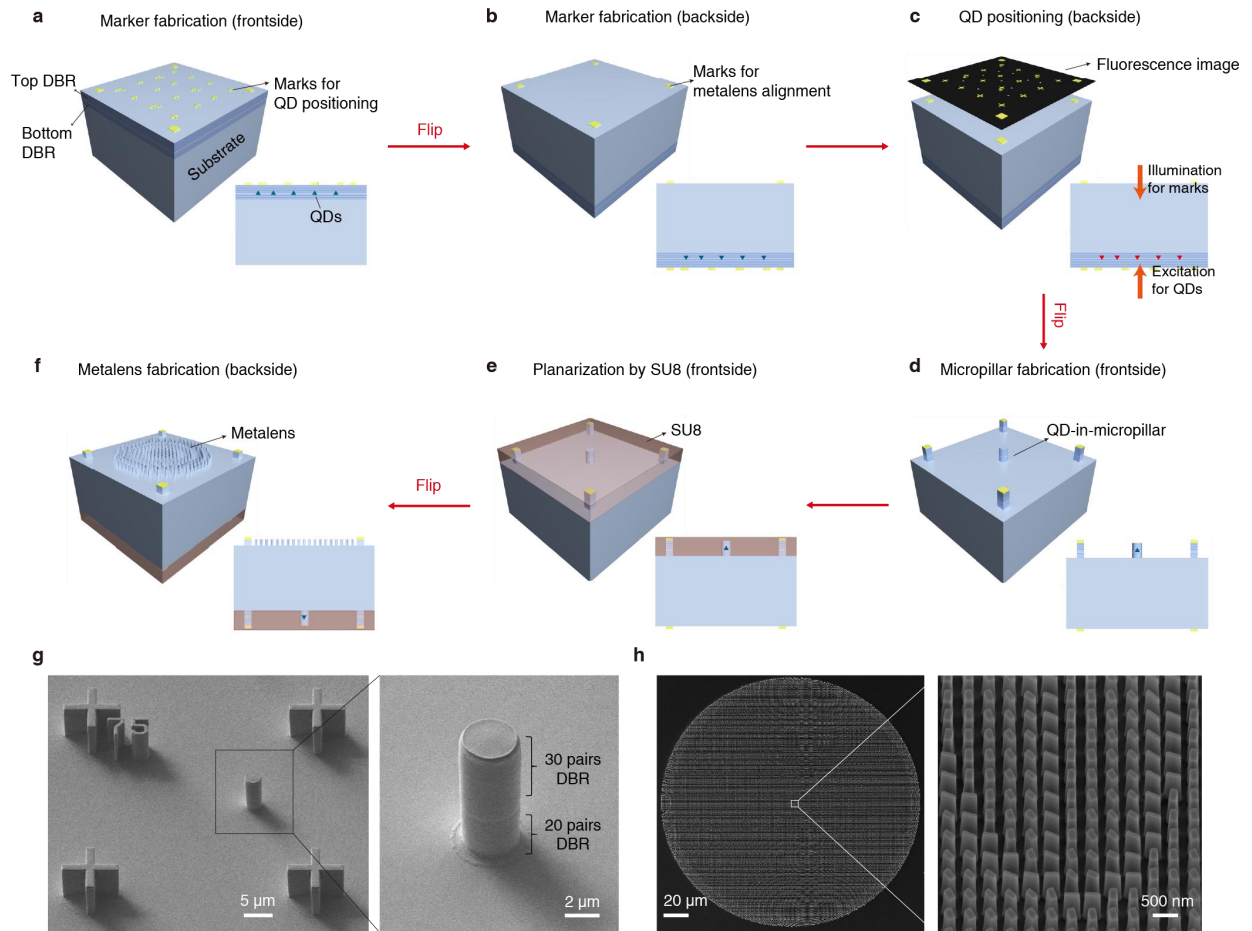


**Fig. 2. Fabrication process of monolithic microcavity-metalens interface.** (a) Fabrication of the front side alignment marks for extracting the positions of QDs. (b) Fabrication of the backside metallic marks to align the metalenses with the front side micropillars. (c) Fluorescence imaging of QDs by illuminating the marks from the back side and exciting the QDs from the front side. The spatial positions of QDs with respect to the front side alignment marks can be extracted from the fluorescence images. (d) Fabrication of the micropillars with QDs in the center by using an aligned EBL and dry etching process. (e) Planarization of front-side micropillars with SU-8 polymer, which protects the micropillars in the fabrication process of metalenses. (f) Fabrication of the backside metalens by another aligned EBL and dry etching process. Insets illustrate the cross-sections in each fabrication step. (g) SEM images of a fabricated front-side micropillar with different magnifications. (h) SEM images of fabricated back-side metalens with different magnifications.

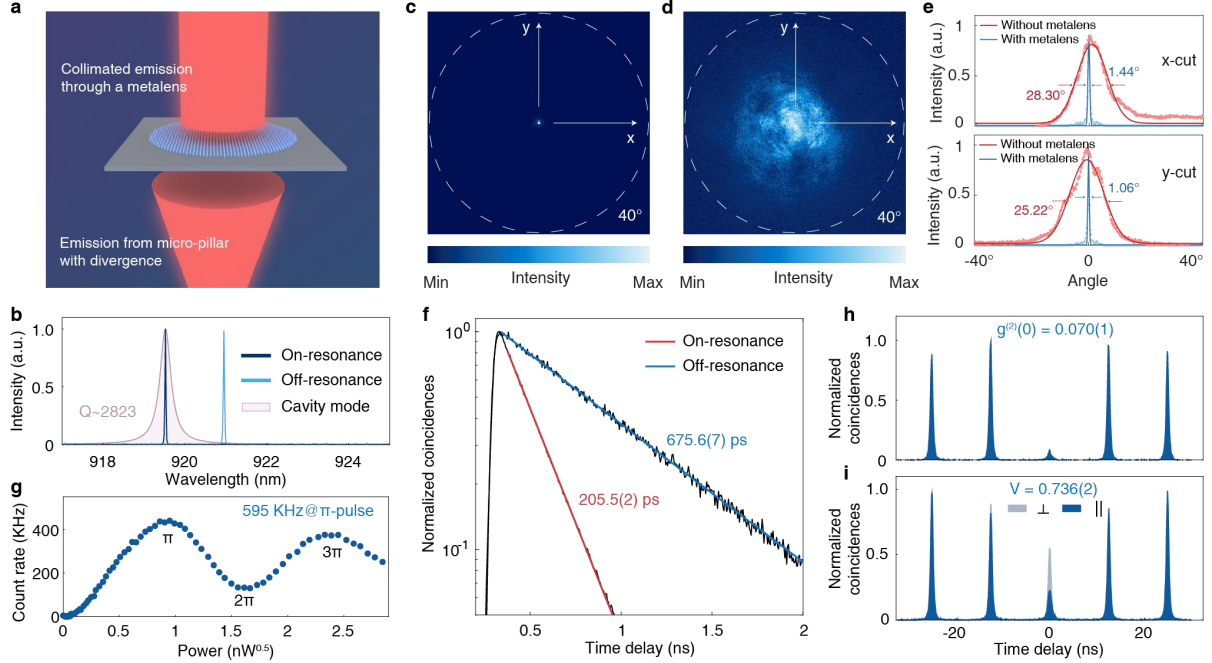


**Fig. 3. Characterization of the metalens-collimated single-photon source.** (a) Schematics of the metalens-collimated single-photon source. A QD in the micropillar emits single photons to the substrate with a divergent angle of  $8.25^\circ$ . The single-photon light beam is collimated by a metalens on the backside, giving rise to collimated single-photon emission. (b)  $\mu$ PL spectra for the QD resonant with and detuned from the cavity mode. (c) Far-field pattern of the collimated single-photon emission. (d) Far-field pattern of a reference single-photon emission without the collimation metalens. (e) Comparison of the cross sections of far-field patterns for the single-photon emission with and without the collimation lens. The one with collimation metalens features a divergence angle as small as  $1.44^\circ$  ( $1.06^\circ$ ) while the single-photon emission without collimation exhibits a large divergence angle of  $28.30^\circ$  ( $25.22^\circ$ ). (f) Lifetimes of the QD when on- and off-resonance to the cavity mode. A spontaneous emission rate enhancement of 3.3 is extracted. (g) Resonance fluorescence intensity as a function of the power of the pulsed excitation laser. Clear Rabi-oscillation is observed, revealing the coherent nature of a quantum two-level system. (h, i) Coincidence histogram of Hanbury-Brown-Twiss (HBT) and Hong-Ou-Mandel (HOM) interferences for the single photons under  $\pi$ -pulsed excitation, giving rise to a  $g^{(2)}(0) = 0.070(1)$  and  $V_{\text{HOM}} = 0.736(2)$ , respectively. The  $g^{(2)}(0)$  is calculated from the integrated area in the zero-delay peak divided by the mean of the peaks away from the zero delay and  $V_{\text{HOM}}$  is calculated from the ratio of the central peak area between the co-polarization and cross-polarization. The  $g^{(2)}(0)$  value is corrected in the extracted  $V_{\text{HOM}}$ .

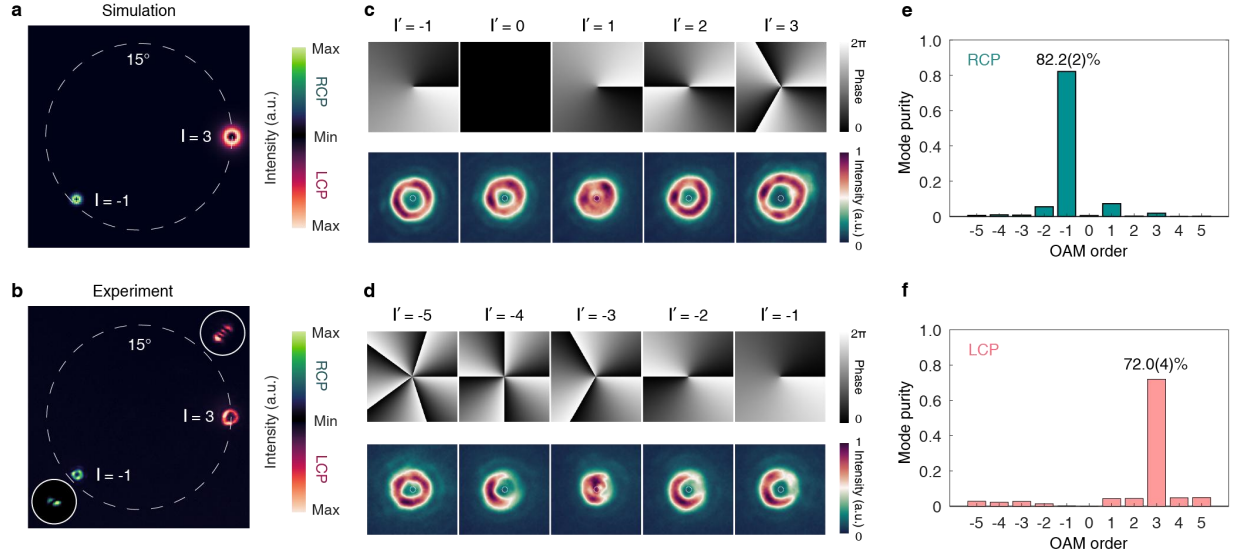


**Fig. 4. Manipulating the photon states of the emitted single photons.** (a) Simulated far-field patterns for the metalens with multi-dimensional functionality. (b) Measured far-field patterns for the metalens with multi-dimensional functionality. Insets in (b) are the interference patterns of the quantum vortices with an offset, clearly revealing the topological charges of the OAM. The topological numbers of the structured single photons are quantitatively extracted with  $L_{RCP} = -1$  and  $L_{LCP} = 3$ . (c,d) Measured far-field profiles of the RCP and LCP channel in (b) by projecting them to a series of vortex wave plates (VWPs) with different topological charge of  $l'$ , respectively. In the bottom panels of (c) and (d), the white dashed circles indicate the central regions used to extract the OAM-mode spectrum. (e,f) Measured OAM mode spectrum of the RCP and LCP channels in (b), respectively. The OAM purities are 82.2(2)% for  $L_{RCP} = -1$  and 72.0(4)% for  $L_{LCP} = 3$ .

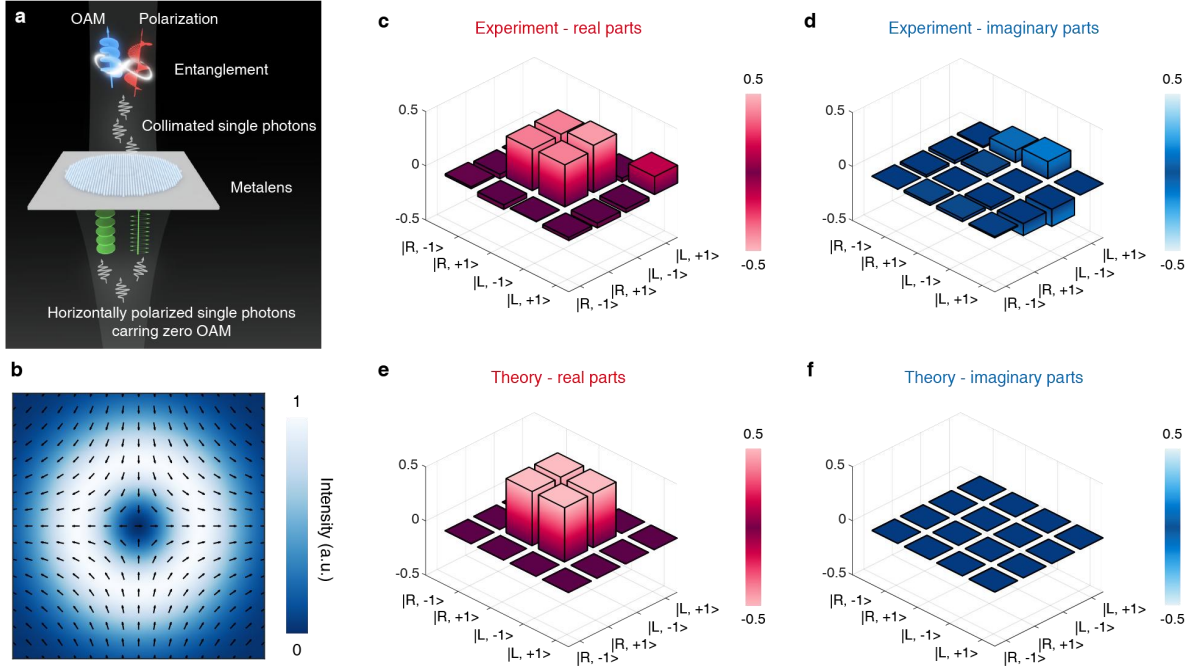


**Fig. 5. Generation of polarization-OAM entanglement with micropillar-metalens interfaces.** (a) Schematic of entanglement between polarization and OAM on a single photon. A horizontally polarized single photon goes into the metalens. This photon carries zero OAM, as illustrated by the green flat phase front. The single photon passes through the metalens and comes out as a single-particle entangled state, depicted as a superposition of the red and blue electric field amplitudes, with the corresponding vortex phase fronts opposite to one another. (b) Intensity and polarization patterns of the Bell state in the combined OAM and polarization space. (c) Real and (d) imaginary parts of the measured density matrix for the state reconstructed via quantum state tomography. The fidelity between the reconstructed state and the theoretical one is equal to  $F = 0.8914 \pm 0.0023$ , where the standard deviation is estimated through a Monte-Carlo analysis assuming a Poissonian statistics. (e) Real and (f) imaginary parts of the density matrix for the ideal polarization-OAM entangled state.

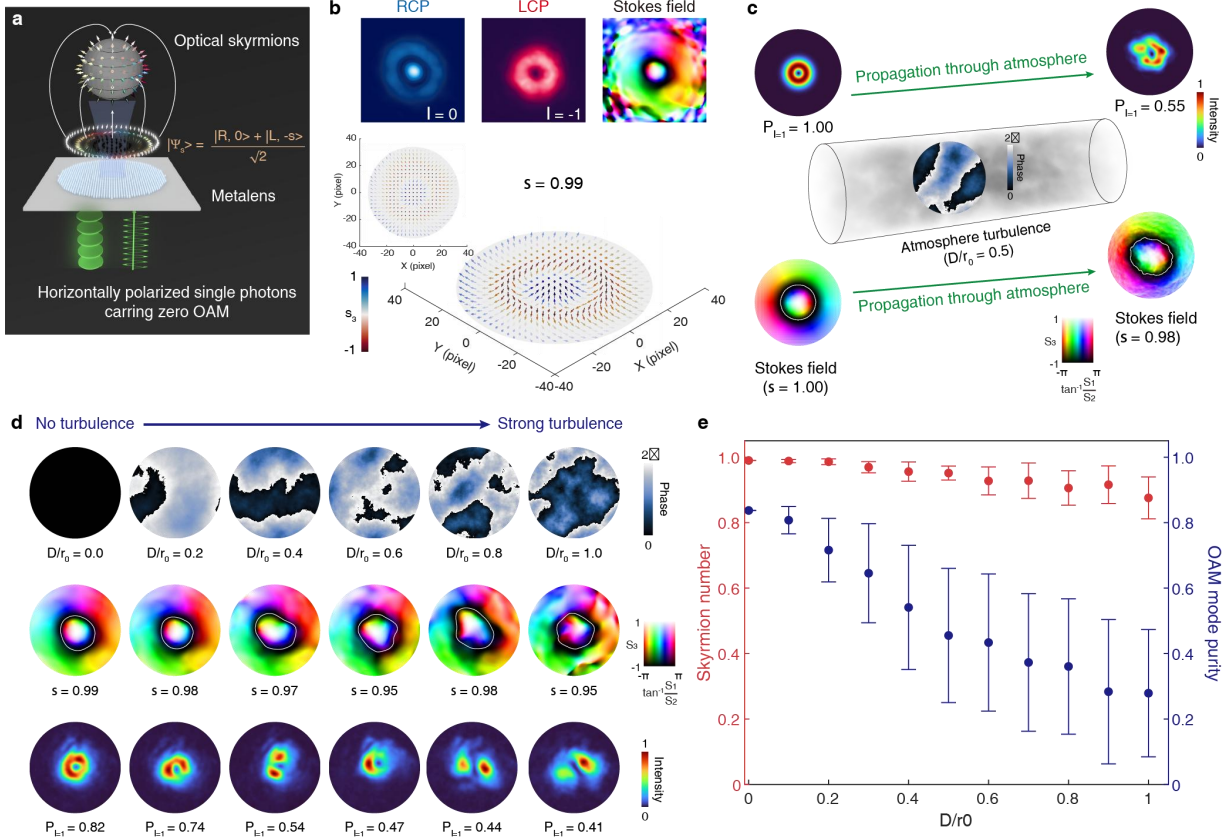


**Fig. 6. Generation of single-photon skyrmions with topological stability by micropillar-metalens interfaces.** (a) Schematic of single-photon skyrmions generated by micropillar-metalens interfaces. (b) The normalized Stokes vector distributions with skyrmion number equal to 1, generated by a simultaneous complex-amplitude-modulation metalens device. The resulting Stokes field exhibits a well-defined skyrmion boundary. Insets in (b) present the measured far-field patterns for the RCP and LCP components and the corresponding Stokes fields. (c) Theoretical model depicting the topological protection of single-photon skyrmions in a turbulent environment. Despite distortions in the Stokes vector field and its skyrmion boundary, the skyrmion number of the Stokes field can still be accurately recovered via boundary identification. (d) Experimentally measured Stokes vector field and the corresponding recovered skyrmion numbers for single-photon skyrmions after propagation through single realizations of atmospheric turbulence with different strengths. (e) Evolution of skyrmion number and OAM mode purity versus turbulence strength  $D/r_0$ , after the single photons with skyrmionic texture ( $s = 1$ ) and OAM ( $l = 1$ ) propagate through atmospheric turbulence, respectively. For each strength of the turbulence, 50 realizations are used in our measurements. These statistics correspond to the error bar. In (b-d) and throughout this paper, the hue and the lightness of the Stokes field pattern represent the different in-plane and out-of-plane components of the Stokes vectors, respectively. While for the vector arrow distributions, the in-plane and out-of-plane components of the Stokes vectors are determined by the direction and color of the arrows.